Nano Energy 78 (2020) 105185

Contents lists available at ScienceDirect

Nano Energy

journal homepage: http://www.elsevier.com/locate/nanoen

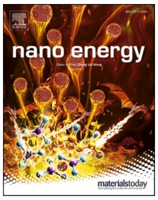

2D intrinsically defective RuO_2/Graphene heterostructures as All-pH efficient oxygen evolving electrocatalysts with unprecedented activity

Yaguang Li [a,b,d,1], Yi Wang [a,b,c,1], Jianmin Lu [a,1], Bing Yang [b], Xingyuan San [d], Zhong-Shuai Wu [a,b,*]

[a] State Key Laboratory of Catalysis, Dalian Institute of Chemical Physics, Chinese Academy of Sciences, 457 Zhongshan Road, Dalian, 116023, China
[b] Dalian National Laboratory for Clean Energy, Dalian Institute of Chemical Physics, Chinese Academy of Sciences, 457 Zhongshan Road, Dalian, 116023, China
[c] University of Chinese Academy of Sciences, 19 A Yuquan Rd, Shijingshan District, Beijing, China
[d] Hebei Key Lab of Optic-electronic Information and Materials, The College of Physics Science and Technology, Institute of Life Science and Green Development, Hebei University, Baoding, 071002, China

ARTICLE INFO

Keywords:
Oxygen evolution reaction
Defective RuO_2
Confined oxygenation
Graphene
Heterostructure

ABSTRACT

Exploring highly active and stable oxygen evolving electrocatalysts is the key for electrochemical water splitting and renewable chemical conversion. RuO_2 is one of the benchmark oxygen evolving electrocatalysts, but remains challenging in high activity in all-pH electrolytes. Herein, we report a confined oxygenation strategy using the finite oxygen species from graphene oxide to synthesize two dimensional (2D) heterostructures of intrinsically defective RuO_2 nanocrystals uniformly grown on graphene (2D D-RuO_2/G), showing ultrathin thickness of 9 nm, high specific surface area of 125 m^2 g^{-1}, enriched hydroxylated surface and notably intrinsic defective RuO_2 with low Ru–O coordination number of 5. Consequently, 2D D-RuO_2/G exhibits a robust stability and an extraordinary oxygen evolution reaction (OER) performance both in acidic and alkaline solutions, achieving a current density of 10 mA cm^{-2} at the overpotential of 169 and 175 mV, and a water oxidation turn over frequency of 1.07 and 1.25 S^{-1} at 270 mV, respectively, corresponding to 344 mV of total overpotential at 10 mA cm^{-2} in acidic and alkaline electrolytes, which greatly exceeds the state-of-the-art of pH-universal OER electrocatalysts. Theoretical studies indicate that intrinsic defective Ru sites can enhance the adsorption and accelerate the decomposition of hydroxyl groups to boost the OER activity. This confined oxygenation strategy provides the opportunities to construct 2D advanced defective OER electrocatalysts in all-pH electrolytes.

1. Introduction

Developing efficient and durable oxygen evolution reaction (OER) electrocatalysts is the key for electricity-driven water decomposition and regenerative fuel cells [1–3]. Specially, RuO_2 is one of the most active catalysts for OER [4,5]. For instance, Mn doped RuO_2 OER catalysts showed 158 mV of overpotential at 10 mA cm^{-2} of OER current density in acidic electrolyte [6], the lowest value in acidic electrolyte reported to date. However, although tremendous efforts have been devoted, the RuO_2 based OER catalysts are not active in alkaline electrolytes, only showing 240 mV of overpotential at 10 mA cm^{-2} [7], far behind the best alkaline OER catalysts (~190 mV at 10 mA cm^{-2}) [8–10]. Therefore, it is urgent to exploit highly active RuO_2 based OER catalysts in both acidic and alkaline electrolytes [11]. Yang et al. have evidenced that the OER activity of RuO_2 was closely related to their defective structures, especially the oxygen defects [12]. It is implied that synthesizing the controllable defected structures might be able to increase the OER activity of RuO_2 in alkaline electrolytes. However, the formation of oxygen defects in RuO_2 is mainly depended on the etching effect of acidic electrolyte rather than alkaline solution [13]. Moreover, in the previous preparation of RuO_2, Ru precursors were completely oxidized by air, H_2O_2, etc. [13], which made Ru full coordinated with oxygens in the as-prepared RuO_2, unable to modulate the defects [14]. To the best of our knowledge, reasonable construction of defective RuO_2 nanostructures to break through the ceiling of alkaline OER performance has never been achieved.

---

* Corresponding author. State Key Laboratory of Catalysis, Dalian Institute of Chemical Physics, Chinese Academy of Sciences, 457 Zhongshan Road, Dalian, 116023, China.

E-mail address: wuzs@dicp.ac.cn (Z.-S. Wu).

[1] These authors contributed equally to this work.

https://doi.org/10.1016/j.nanoen.2020.105185
Received 9 June 2020; Received in revised form 6 July 2020; Accepted 8 July 2020

On the other hand, high electronic conductivity of catalysts is also of great importance for increasing the OER activity [15,16]. However, the pure RuO_2 electrodes usually show high resistance in the order of 2000 Ω [17], which significantly degrades their OER performances. To address this issue, graphene, which is well acknowledged as an excellent two-dimensional (2D) conducting substrate for loading electrocatalysts and fully maximizing the OER performance because of low electrical resistance [18], excellent stability [19], high specific surface area [20]. In particular, 2D ultrathin heterostructures by alternate stacking of metal oxide (*e.g.*, RuO_2) and high-conductive graphene in well-defined sequence would generate a strong synergy, resulting in developed electron-ion conductive frameworks and enriched active sites, synergistically combining the advantages of individual 2D nanosheets to eliminate their drawbacks. Moreover, graphene oxide (GO) having abundant oxygen species (*e.g.*, –OH, –COOH) not only allows uniform anchoring of ultrathin RuO_2 nanosheets via strong covalent interactions of graphene-oxygen-metal bonding [21], but also might precisely tune the coordination structure of metal oxides (*e.g.*, RuO_2) by only using the confined oxygen species from GO nanosheets.

Herein, we report a new strategy of using limited oxygen species from GO as confined oxygen supplier to finitely oxidize the Ru precursor for the formation of 2D heterostructures of intrinsically defective RuO_2 nanocrystals with low Ru–O coordination number of 5, and enriched surface hydroxylation, stably anchoring on graphene (denoted as 2D D-RuO_2/G). Notably, 2D D-RuO_2/G heterostructures present an unprecedented OER electrocatalytic activity not only in acidic electrolyte but also importantly in alkaline solution, showing ultralow overpotential of 169 and 175 mV at 10 mA cm^{-2} in 0.5 M H_2SO_4 and 1 M KOH solution, respectively, outperforming the pH-universal electrocatalyst reported to date [22,23]. The density functional theory (DFT) calculations unravel the intrinsic role of defective Ru sites on significantly improving the adsorption of hydroxyl groups and speed up their decomposition.

2. Experimental Section

2.1. Chemicals

Commercial ruthenium chloride trihydrate ($RuCl_3 \cdot 3H_2O$) and commercial RuO_2 (C–RuO_2) were purchased from Aladdin Co., Ltd. The commercial products were directly used in the followed experiments without any treatment.

2.2. Preparation of 2D D-RuO_2/G

Firstly, 3 mL GO solution (6.7 mg mL^{-1}), synthesized by modified Hummers' method [24], was stirred with 17 mL pure water, followed by adding 10 mg $RuCl_3 \cdot xH_2O$. After stirring for 10 min, the mixture was frozen by using liquid nitrogen (vacuum freeze drying for 3 days). Finally, the obtained sample was tightly wrapped in aluminum foil and heated to 300 °C for 3 h for the formation of the 2D D-RuO_2/G. To determine the content of RuO_2 in 2D D-RuO_2/G, 10 mg 2D D-RuO_2/G was heated to 500 °C for 6 h in air to full oxidize graphene. Remaining RuO_2 was measured to be 7.0 mg, thus the RuO_2 mass ratio in the 2D D-RuO_2/G was 70%.

For comparison, the pure 2D RuO_2 (2D-RuO_2) nanosheets were obtained by annealling the 2D D-RuO_2/G in air at 500 °C for 6 h to remove graphene.

2.3. Characterization methods

Powder X-ray diffraction (XRD, D2 PHASER, BRUKE, Germany) was used to test the phase of samples. JSM-7900F and JEOL 2100F (JEOL, Japan) were applied on obtaining the scanning electron microscopy (SEM) images, transmission electron microscopy (TEM) images, scanning transmission electron microscopy (STEM) and elemental mappings by energy dispersive spectroscopy. Atomic force microscopy (AFM, Cypher ES) was used to detect the thickness of samples. Thermo ESCALAB-250 (Thermo Scientific, USA) with a monochromatic Al Kα radiation source (1486.6 eV) was used to characterize the X-ray photoelectron spectroscopy (XPS) spectra of samples. Micromeritics Tristar 3020 system was used for obtaining the specific surface area and pores distribution of samples. The near Ru K-edge X-ray absorption spectroscopy (XANES) and extended X-ray absorption fine structure (EXAFS) data were tested by the BL14W1 beamline of Shanghai Synchrotron Radiation Facility (SSRF). Athena software was used to calibrate the energy scale, correct the background of signals, and normalize intensity of signals and Fourier transform the data from k-space to r-space.

2.4. Electrochemical measurements

The OER performance measurements were conducted in a three-electrode system on an electrochemical workstation (CHI 760E) in 1 M KOH and 0.5 M H_2SO_4 electrolytes, respectively. The catalyst ink was prepared by ultrasonically dispersing the mixture of 2 mg catalyst, 0.5 mL H_2O, 0.5 mL ethanol, and 5 μL of 5 wt% Nafion solutions. 5 μL of the catalyst ink was pipetted and spread onto a 3 mm diameter glassy carbon electrode. The mass loading of the catalysts was 0.14 mg cm^{-2}. The saturated Ag/AgCl and saturated calomel electrode (SCE) served as the reference electrodes in 1 M KOH and 0.5 M H_2SO_4 electrolytes, respectively. A platinum foil (2.5 cm × 2.5 cm) was used as the counter electrode in the two electrolytes.

All potentials measured were calibrated to the reversible hydrogen electrode (RHE), using the following equation:

$$E_{RHE} = E_{Ag/AgCl} + 0.197\ V + 0.059 \times pH \text{ in 1 M KOH}$$

$$E_{RHE} = E_{SCE} + 0.242\ V + 0.059 \times pH \text{ in 0.5 M } H_2SO_4$$

and the overpotential = E_{RHE} - 1.23 V.

For OER tests, first, the working electrodes were scanned for several potential cycles until the signals were stabilized. Linear scan voltammetry (LSV) measurements were performed at a scan rate of 5 mV s^{-1}. Tafel slopes were calculated based on the LSV curves by plotting overpotential against log (current density). The impedance was very consistent at multiple potential points (covering both non-OER condition and OER-condition). All polarization curves were corrected with 80% *iR*-correction. The electrochemical impedance spectroscopy (EIS) was carried out in a potentiostatic mode, applying a sinusoidal voltage with amplitude of 10 mV and a scanning frequency from 1 MHz to 0.01 Hz.

The C_{dl} was extracted from LSV curves in non-faradaic and OER potential regions at scan rates of 2, 4, 6, 8 and 10 mV s^{-1}. The C_{dl} was estimated by plotting the $\triangle j$ ($j_{anodic} - j_{cathodic}$) against the scan rate. The linear slope is twice the double-layer capacitance C_{dl}.

The TOF value was calculated from the equation: $\kappa = I/(n \times F \times 4)$. *I, n, F* represent the coulomb number of electron quantity per s, the mole number of Ru atoms loaded in electrode, the Faraday constant (96485), respectively.

Δ was the overpotential at the 10 mA cm^{-2} of the electrocatalysts in acid and alkaline electrolytes, respectively. And total overpotential (η) = $\Delta_{acid} + \Delta_{alkaline}$.

2.5. First principle calculations

The Vienna Ab Initio Package (VASP) [25,26] has been used to conduct all the DFT calculations within the generalized gradient approximation (GGA) using the PBE formulation [27]. The projected augmented wave (PAW) potentials [28,29] were chosen to describe the ionic cores and take valence electrons into account using a plane wave basis set with a kinetic energy cutoff of 400 eV. Partial occupancies of the Kohn−Sham orbitals were allowed using the Gaussian smearing method and a width of 0.05 eV. The electronic energy was considered self-consistent when the energy change was smaller than 10^{-7} eV. A geometry optimization was considered convergent when the energy change was smaller than 10^{-6} eV. Grimme's DFT-D3 methodology [30] was used to describe the dispersion interactions among all the atoms in the bulk unit cells and surface models of interest.

The equilibrium lattice constants of rutile RuO_2 tetragonal unit cell were calculated, using a 10 × 10 × 16 k-point grid for Brillouin zone sampling, to be $a = b = 4.505$ Å and $c = 3.113$ Å. This unit cell was used to construct the RuO_2(110) surface with a p (3 × 2) periodicity in the *x*, *y* directions and 2 stoichiometric layers in the z direction, separated by a 15 Å of vacuum in the z direction between the slab and its periodic images. The perfect RuO_2(110) surface contains 48 O and 24 Ru atoms. The gamma point of Brillouin zone was used for *k*-point sampling in the following surface calculations. During structural optimizations, the top O–Ru–O stoichiometric layer was allowed to fully relax while the bottom one was fixed to its bulk position.

3. Results and discussions

The preparation of 2D D-RuO_2/G heterostructures was schematically depicted in Fig. 1a. Firstly, the single-layer GO nanosheets were selected as 2D oxygenated substrates to adsorb ruthenium species (Ru^{3+}) [31]. Subsequently, the solution was freeze-dried for water removal to form Ru^{3+} ions anchored on the GO precursor with 2D discrete nanosheet morphology (Ru^{3+}/GO, Fig. S1). After annealing Ru^{3+}/GO for 3 h at 300 °C isolated by air, 2D D-RuO_2/G heterostructure was finally obtained (See details in Experimental Section). XRD pattern confirmed the existence of rutile RuO_2 (Fig. S2a) [32]. SEM (Fig. 1b) and TEM (Fig. 1c) images revealed the ultrathin transparent nanosheet morphology of 2D D-RuO_2/G heterostructure with a lateral size of a few micrometres. The enlarged TEM image visualized the existence of ultrasmall RuO_2 nanocrystals uniformly grown on graphene (Fig. 1d), and 2D nanomesh-like mesoporous layer. Further, high-resolution TEM (HRTEM) image unveiled the mesoporous layer, which was composed of ultrasmall RuO_2 nanocrystals with a size of around 2 nm, and mainly exposed well-defined *d*-spacings of 0.255 nm, equaling to the rutile RuO_2 (110) plane (Fig. 1e) [33]. Elemental mapping images showed homogeneous distribution of Ru, O and C over the entire nanosheet (Fig. 1f). AFM measurement indicated the ultrathin thickness of ~9 nm (Fig. S2b). In addition, 2D D-RuO_2/G exhibited and mesoporous structure and specific surface area of 125 $m^2\ g^{-1}$ (Figs. S2c and 2d), slightly higher than that of 2D-RuO_2 without graphene (115 $m^2\ g^{-1}$, Fig. S3).

In our case, we used GO as a finite 2D oxygen source to control the oxygen coordination structure of RuO_2 and obtain the intrinsic deficient structures. To demonstrate this, we used the X-ray absorption spectroscopy to characterize the oxygen coordination of 2D D-RuO_2/G heterostructure. As expected, the XANES of 2D D-RuO_2/G resembled the reference spectra of 2D-RuO_2 counterpart (Fig. S4) rather than Ru foil with adsorption edge at 22.126 KeV, indicative of the presence of Ru(IV) in 2D D-RuO_2/G [34]. Fourier transformed-EXAFS (FT-EXAFS) of 2D D-RuO_2/G showed a peak located at 1.5 Å, corresponding to the Ru–O coordination (Fig. 2b) [22]. Further, EXAFS fitting results (Fig. S5, Table S1) identified the Ru–O coordination number of 5 for 2D D-RuO_2/G, compared with 6 for 2D-RuO_2. Hence, it confirms that the intrinsic defective Ru structures have been created in 2D D-RuO_2/G via the GO confined oxygenation strategy. XPS was applied to examine the chemical states of Ru and O at the surface of 2D D-RuO_2/G. Apparently, the similar Ru 3p XPS spectra confirmed the identical chemical state of Ru in both 2D D-RuO_2/G and 2D-RuO_2 (Fig. 2c) [35], consistent with the XANES result. Moreover, the O 1s XPS spectra of 2D D-RuO_2/G and 2D-RuO_2 (Fig. 2d and e) can be split as three components, assigned to the lattice oxygen of RuO_2 (O_{Ru-O}, at 529.1 eV) [36], hydroxyl groups adsorbed on surface of Ru (O_{Ru-OH}, at 531.1 eV) [37], and oxygen bound with carbon (O_{C-O}, at 533.2 eV) [38]. Fig. 2d showed that the

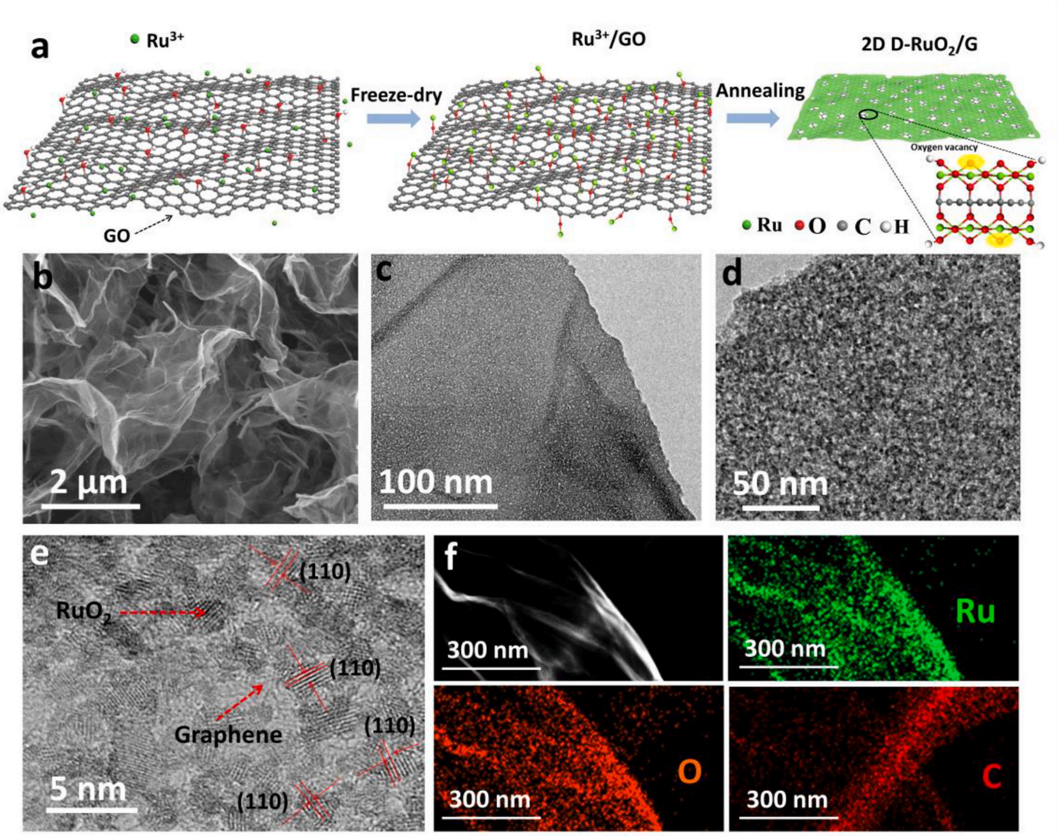

Fig. 1. (a) The sketch of preparation and atomic structure of 2D D-RuO_2/G heterostructures. Green, red, gray and pale spheres present the Ru, O, C and H atoms, respectively. (b) SEM, (c, d) TEM, and (e) HRTEM images of 2D D-RuO_2/G. (f) STEM image and corresponding elemental maps for Ru, O, and C of 2D D-RuO_2/G.

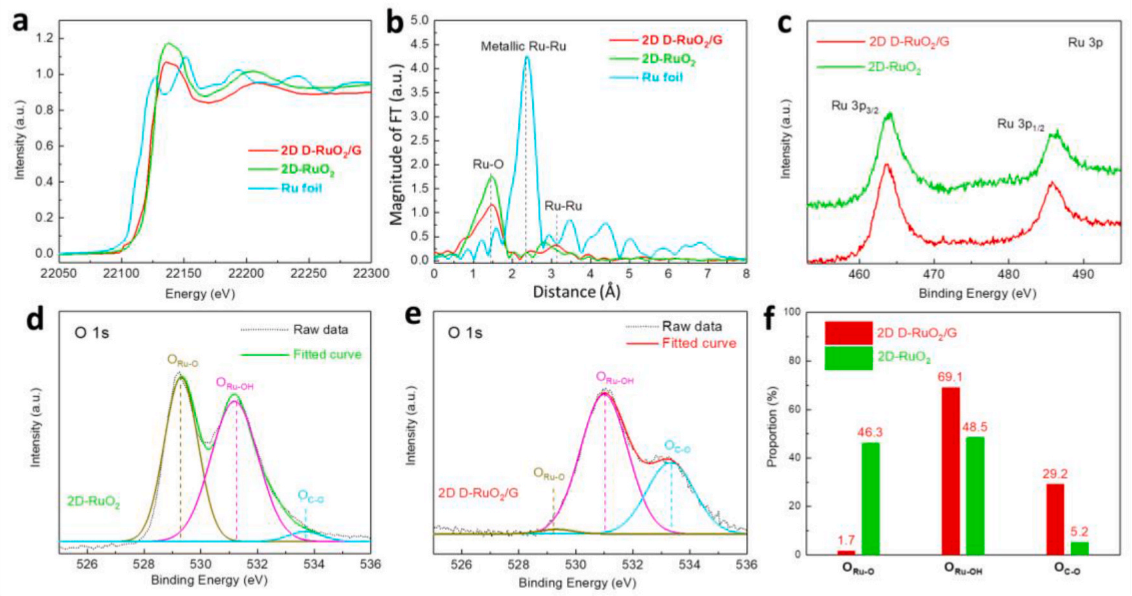

Fig. 2. (a, b) XANES spectra and FT-EXAFS spectra at the Ru K-edge for 2D D-RuO_2/G, 2D-RuO_2 and Ru foil. (c) Ru 3p spectrum of 2D D-RuO_2/G and 2D-RuO_2. (d, e) XPS analysis of the O 1s band for 2D D-RuO_2/G and 2D-RuO_2. (f) The proportion histogram of different oxygen species in 2D D-RuO_2/G and 2D-RuO_2.

percentages of O_{Ru-O}, O_{Ru-OH} and $O_{C\text{-}O}$ at the surface of 2D-RuO_2 were 46.3%, 48.5% and 5.2%, respectively (the $O_{C\text{-}O}$ in 2D-RuO_2 might be originated from the carbon adhesive), while in 2D D-RuO_2/G, O_{Ru-O}, O_{Ru-OH} and $O_{C\text{-}O}$ were 1.7%, 69.1% and 29.2%, respectively (Fig. 2e, the $O_{C\text{-}O}$ in 2D D-RuO_2 might be originated from the graphene and carbon adhesive simultaneously). From this comparison, it was demonstrated that the low-content (1.7%) lattice oxygen and high-content OH^- groups (69.1%) were simultaneously attained in 2D D-RuO_2/G (Fig. 2f), indicating the formation of surface oxygen unsaturated Ru sites of 2D D-RuO_2/G. Such ultrathin 2D D-RuO_2/G nanosheets with low ratio of lattice oxygens and powerful hydroxyl adsorption capacity, have been predicted to substantially boost OER activity [39].

The OER performances of 2D D-RuO_2/G heterostructures were first examined in acidic electrolyte. The double-layer capacitance (C_{dl}) of 2D D-RuO_2/G and 2D-RuO_2 in acidic electrolyte was 102.8 mF cm^{-2} and 11.6 mF cm^{-2}, respectively, revealing the abundant catalytic sites of 2D D-RuO_2/G (Fig. S6). After the stabilization (Fig. S7), 2D D-RuO_2/G showed an overpotential of 169 mV at the polarized current density of 10 mA cm^{-2} (Fig. 3b), which was not only much lower than that of 2D-RuO_2 (289 mV) and C–RuO_2 (300 mV, Fig. S8) but also compared to the reported excellent acidic OER catalysts (Fig. 3c), such as Mn doped RuO_2 (Mn–RuO_2, 158 mV) [6], Co doped RuO_2 (Co–RuO_2, 169 mV) [40], $CaCu_3Ru_4O_{12}$ (171 mV) [22], $Cr_{0.6}Ru_{0.4}O_2$ (178 mV) [3], Zn doped RuO_2 (Zn–RuO_2, 179 mV) [34], Cu doped RuO_2 (Cu–RuO_2, 188 mV) [7],

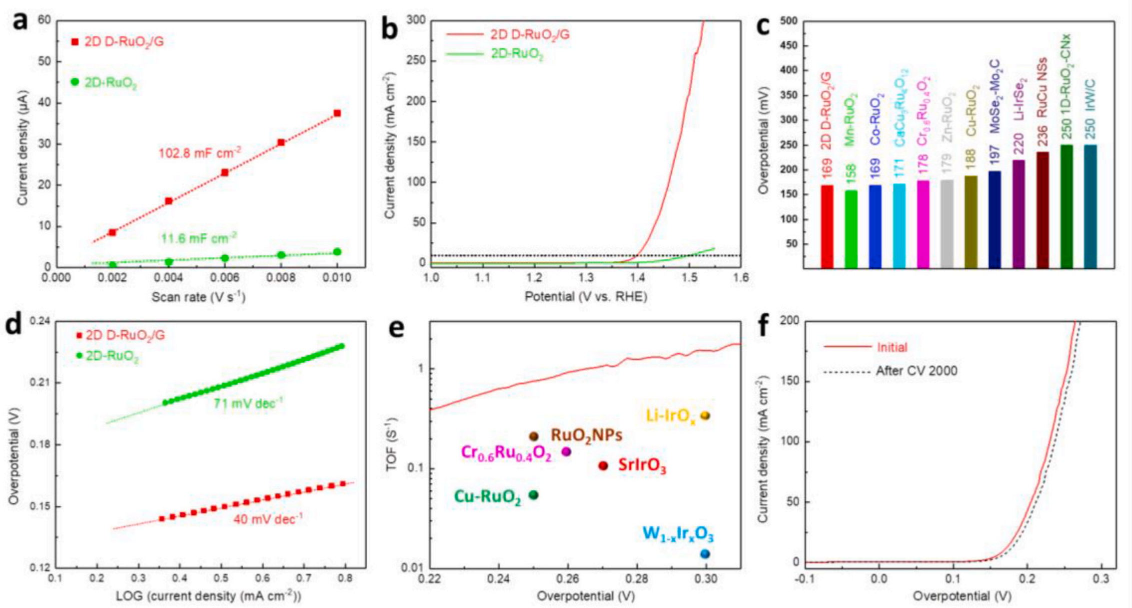

Fig. 3. (a) Capacitive current against the scan rate and corresponding C_{dl} values estimated through linear fitting of the plots. (b) OER polarization curves of 2D D-RuO_2/G and 2D-RuO_2 in 0.5 M H_2SO_4. (c) Comparison of overpotentials at 10 mA cm^{-2} for 2D D-RuO_2/G with previously reported excellent OER catalysts in acidic electrolytes. (d) The Tafel plots of 2D D-RuO_2/G and 2D-RuO_2 in 0.5 M H_2SO_4. (e) The TOF curve of 2D D-RuO_2/G compared with recently reported OER catalysts in acidic electrolytes. (f) OER polarization curves comparison of 2D D-RuO_2/G before and after 2000 CV cycles.

$MoSe_2$–Mo_2C (197 mV) [41], Li–$IrSe_2$ (220 mV) [42], RuCu nanosheets (RuCu NSs 236 mV) [43], 1D-RuO_2-CNx (250 mV) [44], and IrW/C (250 mV) [45]. Note that, we did not refer to the Ni foam based electrocatalysts, due to the high catalysts loading and side reactions. To further highlight the OER activity fairly, the O_2-produced turnover frequency (TOF) of 2D D-RuO_2/G was plotted at the overpotential of 0.22–0.31 V, assuming that all Ru atoms were participated in OER (Fig. 3d). The TOF of 2D D-RuO_2/G at overpotential of 0.27 V was 1.07 S^{-1}, which exceeded the best reported results, *e.g.*, RuO_2 nanoparticles (0.2 S^{-1} at 0.25 V) [32], $Cr_{0.6}Ru_{0.4}O_2$ (0.15 S^{-1} at 0.26 V) [3], Cu–RuO_2 (0.0528 S^{-1} at 0.25 V) [7], $W_{1-x}Ir_xO_3$ (0.13 S^{-1} at 0.3 V) [46], $SrIrO_3$ (0.1 S^{-1} at 0.27 V) [47] and Li-IrO_x (0.32 S^{-1} at 0.3 V) [48]. Such a high TOF value of 2D D-RuO_2/G was not caused by just the ultralow overpotential but also originated from ultrasmall 40 mV·dec^{-1} Tafel slope (Fig. 3e). Moreover, 2D D-RuO_2/G displayed a high durability in acidic electrolyte, showing only 4 mV decay after 2000 cyclic voltammetry (CV) cycles (Fig. 3f).

Besides in acidic electrolyte, 2D D-RuO_2/G heterostructures also revealed a high C_{dl} value of 192.6 mF cm^{-2} in 1 M KOH, indicating its applicability in alkaline electrolyte (Fig. 4a, Fig. S9). Notably, 2D D-RuO_2/G required only an overpotential of 175 mV at the 10 mA cm^{-2} of polarized current density in alkaline solution after stabilization test (Fig. S10), far exceeding the values from 2D-RuO_2 (280 mV, Fig. 4b), C–RuO_2 (401 mV, Fig. S11) and the best Ru based catalysts in alkaline electrolyte (240 mV) [49]. To the best of our knowledge, 2D D-RuO_2/G represented the lowest overpotential among the reported alkaline OER catalysts (Fig. 4c), *e.g.*, NiFeCu alloy (180 mV) [23], FeNiP compounds (180 mV) [8], NiCo-MOF (189 mV) [2], FeCoW gel (191 mV) [1], Cr^{6+}/graphene (197 mV) [9], NiFe/graphene (210 mV) [50], NiFeP alloy (219 mV) [11], NiFe layered double hydroxide/carbon nanotube (NiFe LDH/CNT, 220 mV) [5], RuCu NSs (234 mV) [43], Cu–RuO_2 (240 mV) [7], and $MoSe_2$–Mo_2C (241 mV) [41]. Furthermore, the TOF value of 2D D-RuO_2/G was 1.25 S^{-1} at 0.27 V of overpotential (Fig. 4d), due to the ultralow Tafel slope (37 mV·dec^{-1}, Fig. 4e). The TOF value was at least two-fold higher than reported best values, such as Cr^{6+}/graphene (0.53 S^{-1} at 0.27 V) [9], FeCoW (0.27 S^{-1} at 0.26 V) [1], NiFe LDH/CNT (0.46 S^{-1} at 0.29 V) [5], NiFeOOH (0.09 S^{-1} at 0.25 V) [51], 2D NiSe (0.1 S^{-1} at 0.29 V) [52] and 2D NiFe LDH (0.085 S^{-1} at 0.28 V) [53]. In addition, the OER polarization curves, after 2000 CV cycles, showed a 9 mV decay compared with the initial curve, suggesting excellent durability (Fig. 4f). We listed the reported best pH-universal OER electrocatalysts in Table S2 and it showed that none of the OER electrocatalysts could exhibit excellent overpotential data in both acidic and alkaline electrolytes simultaneously, except the 2D D-RuO_2/G (Table S2). We added up the overpotentials at the 10 mA cm^{-2} (Δ) of the electrocatalysts in acid and alkaline electrolytes as the total overpotential (η). The η of 2D D-RuO_2/G was 344 mV, significantly lower than the previous reported η of Cu–RuO_2 (428 mV) [7], $MoSe_2$–Mo_2C (438 mV) [41], RuCu NSs (470 mV) [43], Li–$IrSe_2$ (490 mV) [42], 1D-RuO_2-CNx (510 mV) [44], and IrW/C (550 mV) [45], which confirmed that 2D D-RuO_2/G heterostructure was the highly efficient, stable pH-universal OER electrocatalysts.

The unprecedented OER activity originated from the unique structural characteristics of 2D D-RuO_2/G nanosheets. Due to the presence of highly conductive graphene in 2D heterostructures, 2D D-RuO_2/G showed low charge transfer resistance of 4.81 Ω in H_2SO_4 electrolyte and 3.75 Ω in KOH electrolyte (Figs. S12a and b), respectively, compared with the 2D-RuO_2 (492 Ω, and 419 Ω) and C–RuO_2 (2287 Ω, and 2003 Ω). Therefore, 2D D-RuO_2/G was able to greatly accelerate the electron transfer of catalysts and increase the OER activity. Moreover, to understand the mechanism of 2D D-RuO_2/G on OER, DFT calculations were carried out (Fig. 5). RuO_2(110), the prominently exposed facet of 2D D-RuO_2/G (Fig. 1f) and the most stable facet of RuO_2, was applied to construct the calculation models (Fig. 5a), in which both five-oxygen coordinated surface Ru at top sites (marked as Ru_0) and six-oxygen coordinated surface Ru at bridge sites co-existed on the pristine (110) plane. It was pointed out that Ru_0 was recognized as the catalytically active site of perfect RuO_2 [7]. Because the OER enhanced mechanism of defective RuO_2 in acid electrolyte was well studied by DFT calculations [54], we used hydroxyl (OH) as reaction intermediate to simulate the OER processes through defective RuO_2 in alkaline electrolyte. As seen from the simulated free energy diagram through Ru_0 (Fig. 5b), the rate-determining step (RDS) from *O to *OOH displayed a potential of +0.77 eV. To simulate the oxygen vacancies and hydroxyls on the surface, we removed the surface lattice oxygen at bridge site partially on

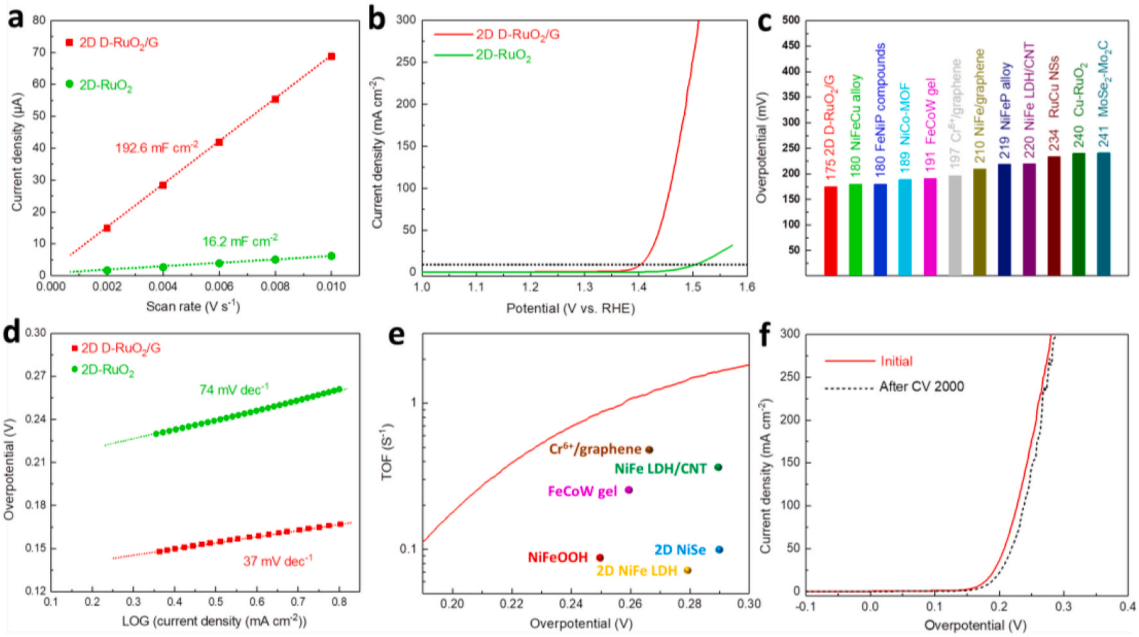

Fig. 4. (a) Capacitive current against the scan rate and corresponding C_{dl} values estimated through linear fitting of the plots. (b) The polarization curves of 2D D-RuO_2/G and 2D-RuO_2 in 1 M KOH for OER. (c) The overpotentials of 2D D-RuO_2/G and the state-of-the-art OER catalysts at 10 mA cm^{-2} in alkaline electrolytes. (d) The Tafel plots of 2D D-RuO_2/G and 2D-RuO_2 in 1 M KOH. (e) The TOF curve of 2D D-RuO_2/G in comparison with reported OER catalysts in alkaline electrolytes. (f) The OER polarization curves of 2D D-RuO_2/G before and after 2000 CV cycles.

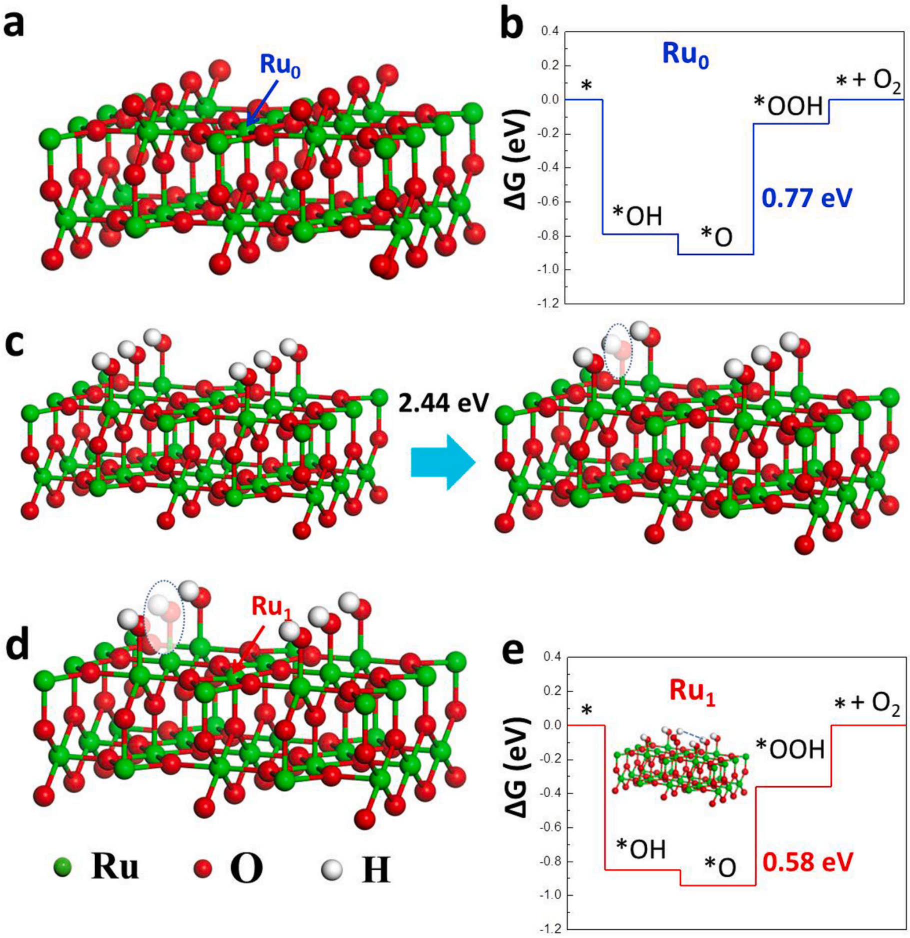

Fig. 5. (a) The side view of perfect $RuO_2(110)$ surfaces. (b) The free-energy profiles of OER on the Ru_0 site. (c) The energy evolution of defective RuO_2 configurations, where the single oxygen is removed from the bridge site. (d) The side view of defective $RuO_2(110)$ surfaces. (e) The free-energy profiles of OER on the Ru_1 site. Green, red and pale spheres present the Ru, O and H atoms, respectively.

$RuO_2(110)$ (Fig. 5c), which was the most stable oxygen defective structure (Fig. S13). On the defective (110) surface, the original Ru_0 was evolved as Ru_1 site with a local asymmetric coordination environment (Fig. 5d). It is calculated that the RDS potential from *O to *OOH was +0.58 eV for Ru_1 site (Figs. 5e), 0.19 eV less than the RDS potential of Ru_0 (+0.77 eV). Bader charge analysis validated that Ru_1 and Ru_0 showed the +1.66 |e| and +1.59 |e| partial charges, respectively. Researchers have confirmed the more positive state, resulting in the higher oxidizing ability and enhanced OER performance of Ru site [34,54]. Further, the oxygen vacancy introduced the asymmetric structure, which strengthened the hydrogen bond from H in *OOH to the nearby coordinated OH group to accelerate the decomposition of *OOH as shown in Fig. 5e. Therefore, the surface defective Ru sites can also enhance the OER activity of RuO_2 in alkaline electrolyte. Particularly, the OER process of RuO_5 structure (donated as Ru_2) located at the bridge site was also theoretically simulated (Fig. S14). It was analyzed that the barrier from *O to *OOH through Ru_2 site was −0.73 eV, which was lower than that on Ru_1 site (+0.58 eV). However, the formed O_2 was barely desorbed from the Ru_2 site due to the bridge geometry. Correspondingly, the O_2 released energy barrier was 3.52 eV that was higher than the RDS potential of Ru_1 site (+0.58 eV), resulting in the inactivity of Ru_2 site for OER.

4. Conclusions

In summary, we developed a finite oxygenation strategy, using oxygen-enriched single-layer GO as a 2D support and a limited oxygen supplier to confine the oxidation of Ru^{3+} precursor, for rational construction of a 2D heterostructure of ultrathin, unsaturated RuO_2 nanocrystals uniformly anchored on conducting graphene. This material is a highly active and durable pH-universal OER catalyst, due to the combined merits of ultrathin thickness, mesopores, high specific surface area, low Ru–O coordination number of 5, and abundant surface hydroxyl groups. Consequently, 2D D-RuO_2/G based OER catalysts achieve ultralow overpotential at 169 and 175 mV for the 10 mA cm^{-2} of current density, the 1.07 and 1.25 S^{-1} of TOF at 1.5 V versus RHE, the 40 and 37 mV·dec^{-1} of Tafel slopes, in H_2SO_4 solution and KOH solution, respectively, constituting the total overpotential of 344 mV. DFT calculations indicate that the bridge site oxygen vacancies on $RuO_2(110)$ surface could significantly enhance the adsorption of oxygen species on the top site Ru atoms and hydrogen dissociation, which substantially reduce the energy barrier of RDS from 0.77 eV to 0.58 eV. Therefore, this present strategy provides a general way to design various 2D heterostructures of unsaturated metal oxides for highly efficient pH-universal electrocatalysis.

CRediT authorship contribution statement

Yaguang Li: Conceptualization, Methodology, Writing - original draft, Funding acquisition. **Yi Wang:** Data curation, Formal analysis, Investigation. **Jianmin Lu:** Software, Validation. **Bing Yang:** Formal analysis, Software. **Xingyuan San:** Data curation. **Zhong-Shuai Wu:** Conceptualization, Supervision, Writing - review & editing, Project administration, Funding acquisition.

Declaration of competing interest

The authors declare that they have no known competing financial interests or personal relationships that could have appeared to influence the work reported in this paper.

Acknowledgements

We thank the founding supporting of National Key R&D Program of China (Grant 2016YFA0200200), National Natural Science Foundation of China of China (Grants 51702078 and 51872283), Liaoning Bai-QianWan Talents Program, Liao Ning Revitalization Talents Program (Grant XLYC1807153), Natural Science Foundation of Liaoning Province, Joint Research Fund Liaoning-Shenyang National Laboratory for Materials Science (Grant 20180510038), DICP (DICP ZZBS201802, DICP ZZBS201708, DICP I202032), DICP&QIBEBT (Grant DICP&QIBEBT UN201702), DNL Cooperation Fund, CAS (DNL180310, DNL180308, DNL201912, and DNL201915). Dr. Y.G. Li acknowledges the Hebei Provincial Department of Education Foundation (Grant No. BJ2019016) and China Postdoctoral Science Foundation (Grant No. 2018M640262). We acknowledge the Shanghai Synchrotron Radiation Facility (SSRF) for conducting the XANES/EXAFS experiment (BL14W1) and thank for the TEM technical supports provided by the Microanalysis Center, College of Physics Science and Technology, Hebei University.

Appendix A. Supplementary data

Supplementary data to this article can be found online at https://doi.org/10.1016/j.nanoen.2020.105185.

References

[1] B. Zhang, X. Zheng, O. Voznyy, R. Comin, M. Bajdich, M. García-Melchor, L. Han, J. Xu, M. Liu, L. Zheng, F.P. García de Arquer, C.T. Dinh, F. Fan, M. Yuan, E. Yassitepe, N. Chen, T. Regier, P. Liu, Y. Li, P. De Luna, A. Janmohamed, H.L. Xin, H. Yang, A. Vojvodic, E.H. Sargent, Science 352 (2016) 333–337.
[2] S. Zhao, Y. Wang, J. Dong, C.-T. He, H. Yin, P. An, K. Zhao, X. Zhang, C. Gao, L. Zhang, J. Lv, J. Wang, J. Zhang, A.M. Khattak, N.A. Khan, Z. Wei, J. Zhang, S. Liu, H. Zhao, Z. Tang, Nat. Energy 1 (2016), 16184.
[3] Y. Lin, Z. Tian, L. Zhang, J. Ma, Z. Jiang, B.J. Deibert, R. Ge, L. Chen, Nat. Commun. 10 (2019) 162.
[4] J. Liu, Y. Ji, J. Nai, X. Niu, Y. Luo, L. Guo, S. Yang, Energy Environ. Sci. 11 (2018) 1736–1741.
[5] M. Gong, Y. Li, H. Wang, Y. Liang, J.Z. Wu, J. Zhou, J. Wang, T. Regier, F. Wei, H. Dai, J. Am. Chem. Soc. 135 (2013) 8452–8455.
[6] S. Chen, H. Huang, P. Jiang, K. Yang, J. Diao, S. Gong, S. Liu, M. Huang, H. Wang, Q. Chen, ACS Catal. 10 (2020) 1152–1160.
[7] J. Su, R. Ge, K. Jiang, Y. Dong, F. Hao, Z. Tian, G. Chen, L. Chen, Adv. Mater. 30 (2018), 1801351.
[8] M. Qian, S. Cui, D. Jiang, L. Zhang, P. Du, Adv. Mater. 29 (2017), 1704075.
[9] Y. Yao, Z. Xu, F. Cheng, W. Li, P. Cui, G. Xu, S. Xu, P. Wang, G. Sheng, Y. Yan, Z. Yu, S. Yan, Z. Chen, Z. Zou, Energy Environ. Sci. 11 (2018) 407–416.
[10] Y. Xu, W. Zhang, Y. Li, P. Lu, Z.-S. Wu, J. Energy Chem. 43 (2020) 52–57.
[11] F. Hu, S. Zhu, S. Chen, Y. Li, L. Ma, T. Wu, Y. Zhang, C. Wang, C. Liu, X. Yang, L. Song, X. Yang, Y. Xiong, Adv. Mater. 29 (2017), 1606570.
[12] R.R. Rao, M.J. Kolb, L. Giordano, A.F. Pedersen, Y. Katayama, J. Hwang, A. Mehta, H. You, J.R. Lunger, H. Zhou, N.B. Halck, T. Vegge, I. Chorkendorff, I.E. L. Stephens, Y. Shao-Horn, Nat. Catal. (2020), 0457.
[13] S. Chen, J. Duan, M. Jaroniec, S.Z. Qiao, Angew. Chem. Int. Ed. 52 (2013) 13567–13570.
[14] H. Over, Chem. Rev. 112 (2012) 3356–3426.
[15] Z. Jian, P. Liu, F. Li, P. He, X. Guo, M. Chen, H. Zhou, Angew. Chem. Int. Ed. 53 (2014) 442–446.
[16] C. Zhang, D. Tang, X. Hu, X. Liu, T. Zhang, H. Zhou, Energy Storage Mater 2 (2016) 8–13.
[17] Y.-F. Xu, Y. Chen, G.-L. Xu, X.-R. Zhang, Z. Chen, J.-T. Li, L. Huang, K. Amine, S.-G. Sun, Nano Energy 28 (2016) 63–70.
[18] H. Long, A. Harley-Trochimczyk, T. Pham, Z. Tang, T. Shi, A. Zettl, C. Carraro, M. A. Worsley, R. Maboudian, Adv. Funct. Mater. 26 (2016) 5158–5165.
[19] M. Liu, R. Zhang, W. Chen, Chem. Rev. 114 (2014) 5117–5160.
[20] D. Deng, K.S. Novoselov, Q. Fu, N. Zheng, Z. Tian, X. Bao, Nat. Nanotechnol. 11 (2016) 218–230.
[21] Z.-S. Wu, D.-W. Wang, W. Ren, J. Zhao, G. Zhou, F. Li, H.-M. Cheng, Adv. Funct. Mater. 20 (2010) 3595–3602.
[22] X. Miao, L. Zhang, L. Wu, Z. Hu, L. Shi, S. Zhou, Nat. Commun. 10 (2019) 3809.
[23] P. Zhang, L. Li, D. Nordlund, H. Chen, L. Fan, B. Zhang, X. Sheng, Q. Daniel, L. Sun, Nat. Commun. 9 (2018) 381.
[24] F. Zhou, H. Huang, C. Xiao, S. Zheng, X. Shi, J. Qin, Q. Fu, X. Bao, X. Feng, K. Müllen, Z.-S. Wu, J. Am. Chem. Soc. 140 (2018) 8198–8205.
[25] G. Kresse, J. Furthmüller, Comput. Mater. Sci. 6 (1996) 15–50.
[26] G. Kresse, J. Furthmüller, Phys. Rev. B 54 (1996) 11169–11186.
[27] J.P. Perdew, K. Burke, M. Ernzerhof, Phys. Rev. Lett. 77 (1996) 3865–3868.
[28] G. Kresse, D. Joubert, Phys. Rev. B 59 (1999) 1758–1775.
[29] P.E. Blöchl, Phys. Rev. B 50 (1994) 17953–17979.
[30] S. Grimme, J. Antony, S. Ehrlich, H. Krieg, J. Chem. Phys. 132 (2010), 154104.
[31] L. Gao, Y. Li, M. Xiao, S. Wang, G. Fu, L. Wang, 2D Mater. 4 (2017), 025031.
[32] E.A. Paoli, F. Masini, R. Frydendal, D. Deiana, C. Schlaup, M. Malizia, T.W. Hansen, S. Horch, I.E.L. Stephens, I. Chorkendorff, Chem. Sci. 6 (2015) 190–196.
[33] Q. Jiang, N. Kurra, M. Alhabeb, Y. Gogotsi, H.N. Alshareef, Adv. Energy Mater. 8 (2018), 1703043.
[34] R. Ge, L. Li, J. Su, Y. Lin, Z. Tian, L. Chen, Adv. Energy Mater. 9 (2019), 1901313.
[35] J. Su, Y. Yang, G. Xia, J. Chen, P. Jiang, Q. Chen, Nat. Commun. 8 (2017) 14969.
[36] Y. Lee, J. Suntivich, K.J. May, E.E. Perry, Y. Shao-Horn, J. Phys. Chem. Lett. 3 (2012) 399–404.
[37] X. Wang, W. Chen, L. Zhang, T. Yao, W. Liu, Y. Lin, H. Ju, J. Dong, L. Zheng, W. Yan, X. Zheng, Z. Li, X. Wang, J. Yang, D. He, Y. Wang, Z. Deng, Y. Wu, Y. Li, J. Am. Chem. Soc. 139 (2017) 9419–9422.
[38] M.S. Romano, N. Li, D. Antiohos, J.M. Razal, A. Nattestad, S. Beirne, S. Fang, Y. Chen, R. Jalili, G.G. Wallace, R. Baughman, J. Chen, Adv. Mater. 25 (2013) 6602–6606.
[39] F. Li, D.-M. Tang, T. Zhang, K. Liao, P. He, D. Golberg, A. Yamada, H. Zhou, Adv. Energy Mater. 5 (2015), 1500294.
[40] Y. Tian, S. Wang, E. Velasco, Y. Yang, L. Cao, L. Zhang, X. Li, Y. Lin, Q. Zhang, L. Chen, iScience 23 (2020), 100756.
[41] L. Najafi, S. Bellani, R. Oropesa-Nuñez, M. Prato, B. Martín-García, R. Brescia, F. Bonaccorso, ACS Nano 13 (2019) 3162–3176.
[42] T.T. Zheng, C.Y. Shang, Z.H. He, X.Y. Wang, C. Cao, H.L. Li, R. Si, B.C. Pan, S. M. Zhou, J. Zeng, Angew. Chem. Int. Ed. 58 (2019) 14764–14769.
[43] Q. Yao, B. Huang, N. Zhang, M. Sun, Q. Shao, X. Huang, Angew. Chem. Int. Ed. 58 (2019) 13983–13988.
[44] T. Bhowmik, M.K. Kundu, S. Barman, ACS Appl. Mater. Interfaces 8 (2016) 28678–28688.
[45] F. Lv, J. Feng, K. Wang, Z. Dou, W. Zhang, J. Zhou, C. Yang, M. Luo, Y. Yang, Y. Li, P. Gao, S. Guo, ACS Cent. Sci. 4 (2018) 1244–1252.
[46] S. Kumari, B.P. Ajayi, B. Kumar, J.B. Jasinski, M.K. Sunkara, J.M. Spurgeon, Energy Environ. Sci. 10 (2017) 2432–2440.
[47] L.C. Seitz, C.F. Dickens, K. Nishio, Y. Hikita, J. Montoya, A. Doyle, C. Kirk, A. Vojvodic, H.Y. Hwang, J.K. Norskov, T.F. Jaramillo, Science 353 (2016) 1011–1014.
[48] J. Gao, C.-Q. Xu, S.-F. Hung, W. Liu, W. Cai, Z. Zeng, C. Jia, H.M. Chen, H. Xiao, J. Li, Y. Huang, B. Liu, J. Am. Chem. Soc. 141 (2019) 3014–3023.
[49] J. Creus, J. DeTovar, N. Romero, J. García-Antón, K. Philippot, R. Bofill, X. Sala, ChemSusChem 12 (2019) 2493–2514.
[50] X. Long, J. Li, S. Xiao, K. Yan, Z. Wang, H. Chen, S. Yang, Angew. Chem. Int. Ed. 53 (2014) 7584–7588.
[51] L. Trotochaud, J.K. Ranney, K.N. Williams, S.W. Boettcher, J. Am. Chem. Soc. 134 (2012) 17253–17261.
[52] H. Wu, X. Lu, G. Zheng, G.W. Ho, Adv. Energy Mater. 8 (2018), 1702704.
[53] F. Song, X. Hu, Nat. Commun. 5 (2014) 4477.
[54] C.F. Dickens, J.K. Nørskov, J. Phys. Chem. C 121 (2017) 18516–18524.

Yaguang Li received his BS degree in Materials Science and Engineering from Yanshan University in 2010 and his Ph.D. in Materials Physics and Chemicals from Zhejiang University in 2015. Then he joined the College of Physics Science and Technology of Hebei University, and currently is an associate professor. Since 2018, Dr. Li is working as a postdoctoral fellow at Dalian Institute of Chemical Physics (DICP), CAS. Currently, Dr. Li's research interests include the synthesis of novel graphene based 2D materials and related heterostructures, photothermal catalysis, and electrocatalysis.

Yi Wang received her B.S. degree in Applied Chemistry from Nanjing Normal University in 2019. She is pursuing a Ph.D. degree from DICP, CAS, under the supervision of Prof. Zhong-Shuai Wu. Her research interests concentrate on graphene and 2D materials for catalysis.

Jianmin Lu received his Ph.D. from the Institute for Metal Research, CAS in 2007 and worked as a postdoctoral fellow first in CAMD, Technical University of Denmark, Denmark from 2007.11 to 2008.11, and then in the University of South Carolina, USA from 2008.12 to 2014.11. Since March 2015, Dr. Lu worked as an associate professor in the DICP, CAS. His current research interests include density functional theory calculations on various catalytic topics, such as biomass conversion, CO_2 reduction, C1 chemistry, electro-catalysis etc.

Bing Yang received his Ph.D. from the Institute of Physics, CAS in 2010 and worked as a postdoctoral fellow at Fritz-Haber Institute of Max Planck Society in Berlin, Germany and Argonne National Laboratory, US. He is currently an associate professor at DICP, CAS. Dr. Yang's research interests include surface chemistry and catalysis, in situ microscopy and spectroscopy for catalysis, dynamic restructuring of catalyst during reaction.

Xingyuan San graduated from Kunming University of Science and Technology in 2011, and received his Ph.D. from University of Chinese Academy of Sciences in 2017. He is currently a lecturer of Physics Science and Technology at Hebei University, China. His research interests include transmission electron microscopy and the applications in materials science. He is especially interested in analyzing and understanding the defect structures of solid state materials and interfaces at atomic level.

Zhong-Shuai Wu received his Ph.D. from the Institute for Metal Research, CAS in 2011 and worked as a postdoctoral fellow at the Max Planck Institute for Polymer Research in Mainz, Germany from 2011 to 2015. Subsequently, Dr. Wu became a full Professor at DICP, CAS, and was promoted as a DICP Chair Professor in 2018. He is a Group leader of 2D Materials Chemistry & Energy Applications, affiliated with State Key Laboratory of Catalysis. Currently, Prof. Wu's research interests include the energy chemistry of graphene and 2D materials, surface- and nanoelectrochemistry, microscale electrochemical energy storage, supercapacitors, batteries and catalysis. He is an editor of *Applied Surface Science*, the 2018 and 2019 High Cited Researchers (Clarivate Analytics), and the Fellow of the Royal Society of Chemistry.